

Influence of re-melting on surface roughness and porosity of AlSi10Mg parts fabricated by selective laser melting

Yu, Wenhui; Sing, Swee Leong; Chua, Chee Kai; Tian, Xuelei

2019

Yu, W., Sing, S. L., Chua, C. K., & Tian, X. (2019). Influence of re-melting on surface roughness and porosity of AlSi10Mg parts fabricated by selective laser melting. *Journal of Alloys and Compounds*, 792, 574-581. doi:10.1016/j.jallcom.2019.04.017

<https://hdl.handle.net/10356/143175>

<https://doi.org/10.1016/j.jallcom.2019.04.017>

© 2019 Elsevier B.V. All rights reserved. This paper was published in *Journal of Alloys and Compounds* and is made available with permission of Elsevier B.V.

Downloaded on 09 Apr 2024 14:21:58 SGT

**Influence of re-melting on surface roughness and porosity of AlSi10Mg parts fabricated
by selective laser melting**

Wenhui Yu^{1, 2, 3}, Swee Leong Sing², Chee Kai Chua^{2*}, Xuelel Tian^{1*}

¹ Key Laboratory for Liquid-Solid Structural Evolution and Processing of Materials, Ministry
of Education, Shandong University, Jinan 250061, P.R. China

² Singapore Center for 3D Printing, School of Mechanical and Aerospace Engineering,
Nanyang Technological University, 50 Nanyang Avenue, 639798, Singapore

³ School of Mechanical Engineering, Shandong University of Technology, Zibo 255000, P.R.
China

ABSTRACT

Re-melting strategies with same and opposite directions to the first scanning routine were performed in AlSi10Mg parts by selective laser melting (SLM) technology. Surface roughness and porosity were investigated with confocal microscopy, micro-computed tomography (CT) and optical microscopy (OM). Re-melting facilitates the top surface finish with Ra value decreasing from 20.67 μm to 11.67 μm (same direction) and 10.87 μm (opposite direction), almost at the same level. On side surface there is a contradictory trend. Pores at SLM parts include spherical pores due to entrapped gases, irregular pores for lack of fusion, and keyhole pores because of laser movement. The former two kinds form in the central areas while the latter one is located at edges of melting tracks and exhibits different distribution at both sides. Re-melting allows more chances for pores (spherical and keyhole

*Corresponding author.

E-mail address: mckchua@ntu.edu.sg (C.K. Chua), tianxuelel@sdu.edu.cn (X.L. Tian).

pores) to escape from the melting pools. Irregular pores decrease because smoother surface allows powders to be fully melted. Porosity decrease of both re-melting strategies in central areas of the SLM parts is almost on the same level while same directional re-melting exhibits superior ability to release porosity at edges because of the porosity distribution difference at the head and wake of the melting tracks.

Keywords: Selective laser melting; Re-melting; Surface roughness; Porosity

1. Introduction

Additive manufacturing (AM) technologies are coming of age and have been continuously improved for decades. The techniques gain their popularity because they enable high freedom of complex components, efficient usage of materials and elimination of expensive molds [1-3]. Among various AM technologies, selective laser melting (SLM) has emerged as a promising technique for metals and alloys fabrication since 1980s [4]. Laser scans and melts the powder materials layer by layer according to three-dimensional (3D) models, enabling high cooling rate and fine grain structure. Despite numerous advantages of the new technology, problems always accompany. The surface roughness and densification of the SLM fabricated parts remains to be improved [5]. Materials and parameters selection is the main consideration to improve the quality of parts. Various materials have been tried with SLM [6], whereas the alloys that can be reliably printed are limited. Therefore, additions of grain refiners such as scandium [7] and various nanoparticles [8, 9] are considered to improve the processing ability of alloys. On the other hand, parameters, such as laser power, scanning speed, hatch space, layer thickness and scanning strategies, have been well investigated and optimized for each material [10-12]. Among these schemes, re-melting strategy, in which the same slice is scanned twice or more times before recoating powders, offers a solution to improve the quality of parts. The applications and challenges of this technique have been well reviewed [13]. It is well established that laser surface re-melting contributes to the improvement of surface finish [14]. In addition, the effect of higher cooling rate in re-melting routines to refine grains was calculated and observed [15-20]. High hardness, corrosion resistance [21] and even amorphous phase [22] can therefore be achieved with laser surface

re-melting. The reduction of cracks and porosities [18] after surface re-melting offers possibility of densification improvement with re-melting on every layer. This method is less popular due to the expense of longer building time. However, it can be the ultimate solution for applications in demand of high densification. The influence on densification depends on the first and subsequent laser scanning parameters, which can offer a whole lot of freedom for the SLM process. Yasa et al. [23, 24] utilized laser re-melting on stainless steel 316L and Ti6Al4V alloys to investigate the influence of re-scanning parameters, such as scanning space, scanning speed, laser power and number of re-melting scans. Scanning speed was demonstrated to be the most effective parameter to achieve near-full density parts. The research of Cu-Al-Ni-Mn shape-memory alloy by Gustmann et al. [25] confirms the results of Yasa. AlMangour et al. [26] performed re-melting strategies on nanocomposites and revealed that it improved the densification of the parts from 92.48 % to 96.04 %. Besides, it caused redistribution of nanoparticles although the principle was not discussed. Microstructure can be modified by re-melting due to high cooling rate of the overall parts [25]. Some researchers [27, 28] regard re-melting as an unfavorable strategy when laser power is too high as higher cooling rate results in higher residual stress and stronger texture. However, with several number cycles of re-melting, residual stress could be reduced with increasing temperature of solidified layers and lower thermal gradients in re-melting zones. Zhang et al. [29] reported that overlap area in multi-laser selective laser melting presents no obvious difference in grain size, indicating that re-melting has little influence on microstructure. This may be attributed to the same parameters of the isolated and overlap areas. Other researchers utilized re-melting from special prospective. Weingarten et al. [30] employed low power laser scanning as an

efficient method in the first routine to dry the powder materials in order to minimize hydrogen porosity. Vaithilingam et al. [31] revealed the effects of re-melting on surface chemistry in elemental composition and the thickness of surface oxide layer. In situ heat treatment can be achieved by re-melting [21, 32]. Nevertheless, the influence of re-melting direction was rarely investigated.

Aluminum (Al) alloys are suited for eco-designed components due to their low weight and superior mechanical and chemical properties. Ultimate tensile strength (UTS) of Al alloys witnesses a significant increase over that of alloys fabricated by conventional methods although plasticity decreases [33]. Corrosion resistance of SLMed alloys is also improved especially compared with castings [34]. Al-Si, Al-Mg, Al-Zn-Mg alloys have been tried to be fabricated with SLM technique [33-35]. The main drawbacks of Al alloys lies in their low absorptivity to laser beam and high susceptibility to oxygen. Hence, most Al alloys show lower effectiveness of SLM processing than Titanium (Ti) and Nickel (Ni) based alloys. AlSi10Mg alloy is popular among the various alloys in SLM processing due to its near eutectic composition and small range of solidification. Minor additions of Mg enable precipitation of Mg_2Si and thus hardenability by natural or artificial ageing [36, 37]. Therefore, in the scope of this study, AlSi10Mg alloy was used to reveal the influence of re-melting strategies with different directions on surface roughness and porosity.

2. Experimental procedures

2.1 SLM processing

The commercial spherical AlSi10Mg powder supplied by TLS Technik GmbH & Co. Spezialpulver KG, Germany is depicted in Fig. 1 with a diameter range between 20 and 63

μm . Cuboids of $10 \times 10 \times 10 \text{ mm}^3$ were produced on a SLM 280 HL machine equipped with two 400 W lasers of 1064 nm wavelength. The fabrication of the samples was carried out in an argon atmosphere with less than 0.05 % oxygen. The building platform was preheated at 200 °C. Scanning strategies are illustrated in Fig. 2. The blue arrows represent the contour scanning, which is scanned only once. The raster scanning is marked by the green and orange arrows, indicating the first and second routine within the same layer, respectively. The other processing parameters listed in Table 1 follow the recommendation of the machine maker. Five cubes for each group were fabricated.

2.2 Surface roughness

The measurements of average surface roughness (R_a) on top (top xoy plane in Fig. 3) and side surface (xoz plane in Fig. 3) were performed using the VK-X200 3D laser scanning confocal microscope by Keyence. Confocal microscopy offers several advantages over conventional wide field optical microscopy, including the ability to control depth of field and elimination or reduction of background information away from the focal plane. Five groups of data were obtained for each sample.

2.3 Porosity analysis

A micro-CT scanner (Brucker Skyscan 1173) was used to scan the parts at 80 kV voltage and 90 μA current to collect 2D slice image data. X-ray was filtered with a 2-mm thick Al filter to reduce beam hardening artefacts. Considering the resolution and the penetration ability of X-ray into the dense metallic parts, only the upper 1/3 part was scanned for each sample. The cutting plane is marked in Fig. 3. CTRecon software was used to reconstruct the 3D models of the scanned parts through the 2D slice image data. CTAn software was

subsequently employed to attain the distribution and porosity (volume fraction). OM images of vertical and horizontal cross sections to the building plane were obtained to reveal the 2D distribution and position of pores at edges and centers of the parts.

3. Results and discussion

Fig. 4 plots the change of surface roughness at top and side surfaces of the samples with different scanning strategies. Ra value of Sample 1 on top surface reaches up to 20.67 μm , and drops to 11.67 μm and 10.87 μm for Sample 2 and 3, respectively. 3D display of top surface profiles and corresponding microstructure (Fig. S1) present that re-melting strategies help to smooth top surfaces. On the surface of Sample 1 are some bumps which refer to the un-melted or partially melted particles (Fig. S1a), indicated by the ellipse and arrow in Fig. S1d. Sample 2 and 3 show flatter surfaces with much less and lower bumps (Fig. S1b-c, e-f). Insets in Fig. S1d-f are the macro photos of top surface. Compared with the dark and rough surface of Sample 1, smooth surfaces with metallic luster of Sample 2 and 3 imply that re-melting leaves less oxidation after solidification. It is understandable that the residual particles are melted in the second scanning routine, which facilitates finer top surface finish significantly. Note that re-melting also reveals surface with metallic luster and clear tracks (Fig. S1). Powder materials introduce more surfaces and thus exposes larger surface of Al alloys to oxygen although the chamber is argon-shielded with only 0.05% oxygen. On the other hand, powder materials absorb more laser energy and achieve higher temperature, making Al more sensitive to oxygen. Therefore, the oxidation of re-melting tracks is less severe. In the first scanning process, the oxidation films mainly form and float on the surfaces of the melting pools, while in the second routine, oxidation films are broken, revealing new

surfaces [38]. This also accounts for the smoother and more lustrous surface. As re-melting scanning breaks the oxidation films, some of them are enrolled into the re-melting pools inevitably. This implies that the mechanical properties would be affected to some extent. According to our previous research [39], Sample 2 and 3 shows inferior performance to Sample 1 with regard to UTS. The inclusion of oxide films may account for part of the degradation [40]. However, significant increase in elongation was witnessed after re-melting [39]. This is because the re-melting introduces self-heat-treatment. The microstructure in Fig. S2 shows that re-melting helps to generate more heat affected zone (the area between the dotted lines). More silicon is transformed to granular particles. Ra values of side surfaces (xoz plane) show a contradictory trend after re-melting. Partially fused powders tend to adhere on the side surfaces of the parts [41]. In the re-melting routine, more powders are exposed to melting pools, and the partially fused powders in the first routine tend to expand because of heat absorption [42], leading to a rougher surface. These two re-scanning directions seem to reveal no obvious difference upon surface roughness.

Fig. 5 shows the melting pool profiles of the three samples. The distance (d) between melting pool bottoms of adjacent layers varies most in Samples 1, in which some large melting pools distribute randomly. The d value (measured by at least 3 images with over 300 melting pools) can be as large as 142.29 μm . The average value of d is 60.8 (± 28.2) μm while the layer thickness was set as 50 μm . Large melting pools are supposed to form by submerging the former ones, thus making the bottom of melting pools among adjacent melting tracks not aligned. This phenomenon is due to the uneven distribution of powder materials. As the layer thickness is 50 μm and the powder size is between 20 and 63 μm , the

deposited powder layer could be one to two layers of spherical powders. The areas where there are more powders in number absorb higher laser energy. Deeper melting pools are thus generated.

Although there are also some melting pools exhibiting d over 100 μm in Sample 2 and 3, the melting pools distribute more uniformly. Because in the re-melting process laser scans the bulk materials, laser absorptivity is more uniform within different areas. Laser instability is also considered to explain the uneven distribution of melting pools. However, it is supposed to be the same within the first and second routine. Hence, the state of materials remains the main cause for the change of melting pools redistribution. The average d size is 47.5 (± 21.8) μm and 44.5 (± 21.8) μm for Sample 2 and 3, respectively. The scanning on powder and bulk materials generates melting pools of different size due to the different laser absorptivity and thermal properties especially thermal conductivity. Thermal conductivity of powder materials depends on the initial porosity of the powder bed [43], lower than that of bulk materials. Less heat absorption and rapid heat dissipation in bulk materials result in shallower melting pools. The average number of the melting pools in one column in the three samples is 17, 22, and 23, respectively. Although re-melting generates more melting pools, the increase in number is far from double, which means that the size of re-melting pools resembles that of the former ones and cannot be distinguished well.

The porosity distribution of the three samples is visualized in Fig. 6, reconstructed from micro-CT images. All figures are viewed from top, among which Fig. 6a, b and c are in perspective view and Fig. 5d, e and f are in parallel view. At the first glance, pores distributed mainly at edges of each sample, with bigger size than those in central areas of the parts.

Re-melting strategies induce significant decrease of porosity both at the central areas and edges. Insights into top view (Fig. 6d, e and f) reveal that there is a gap between pores at edges. It is easy to understand that the gap forms because of contour scanning. Inside the gap is continuous distribution of pores in the raster scanning. In the present work, only pores in raster scanning will be discussed. The delamination indicates the scanning tracks of adjacent layers. Due to the bi-directional scanning strategy for Sample 1, the distribution of pores varies between adjacent tracks. In Fig. 6d, the size and number of pores at each side show an alternative distribution, indicating the different influence at the head and wake of the laser beam. The bi-directional distribution is less visible after re-melting, especially in Fig. 6e.

Fig. 7 depicts the porosity of total and central areas of the samples. Both of them exhibit a decreasing trend after re-melting. Porosity of total areas decreases from 0.154% (Sample 1) to 0.0696% (Sample 2) and 0.0918% (Sample 3). Sample 3 with opposite re-melting direction shows higher total porosity while in the central areas the porosity is on the same level with Sample 2. The results mean that opposite directional re-melting leaves more pores at edges.

To observe the distribution of pores more precisely, OM images of top/side views were obtained (Fig. 8 and Fig. 9). Fig. 8 shows the OM images at edges of the horizontal section to top surface. Contour scanning and raster scanning were separated by dashed lines. The distribution features depicted by micro-CT can be observed in Fig. 8a while it becomes inconspicuous in Fig. 8b and c. Large sized pores in the raster areas accumulate at the starting and ending points. The pores at edges may arise by significant local overheating during the laser's return movement, creating keyhole melting pools [44]. Keyhole pores inside the deposit consist of entrapped vapor [45] and are almost spherical in shape [46]. Since the

keyhole equilibrium is very sensitive, the keyhole becomes easily unstable and will collapse, thereby creating large pores.

Fig. 9a, b and c shows the porosity distribution in central areas of Sample 1, 2 and 3 from side view, while Fig. 9d, e and f presents the information from top view. These figures illustrate two main types of pores, i.e. irregular and spherical pores. In Fig. 9a, irregular pores accumulate at between the neighboring tracks (indicated by the white arrows) while spherical ones distribute inside the melting pools (indicated by the orange arrows). Melting tracks in Fig. 9d are separated by dash lines to further reveal the porosity distribution. Irregular pores are supposed to form due to lack of fusion. Considering the spherical shape, the second kind of pores may attribute to the entrapment of the shielding gas inside the melting pools. Argon gas was employed as shielding gas to prevent contamination of the melting pools. It is known that inert gasses are insoluble in liquid metals [47], so any pores created will remain in the solidified pool unless they can escape by floating out of the melting pools. Besides, the hydrogen dissolved in the powder can be degassed and trapped [48]. Fig. 9 shows that both irregular and spherical pores exhibit a decreasing trend in size and number after re-melting.

The principles of porosity release at edges and central areas are illustrated in Fig. 10 and Fig. 11, respectively. The porosity distribution at edges of each routine is illustrated in Fig. 10. According to the micro-CT information, the head and wake of the melting track show different trends of porosity distribution. Re-scanning results in less heat absorption, rapid heat dissipation and thus less keyhole mode melting pools [49, 50]. In this case, keyhole pores at re-melting routines are smaller and distribute nearer to the end of melting tracks. Similar distribution of keyhole pores at second and first routine means similar distribution of melting

pool shapes and higher efficiency of pores release. Blue circles in Fig. 10 represent the partially released pores because of insufficient penetration of the re-melting pools. According to Fig. 10b, the difference between the head and wake of the melting track is inclined to decrease after same directional re-scanning. For parts with opposite re-melting strategy, the size and shape of melting pools at edges differ from the previous one. The release of existing pores is thus insufficient, leaving more pores at edges of Sample 3 (Fig. 10c).

In the central areas, when the powders were melted, argon gas, hydrogen and gas between the powders are entrapped in the melting pools, creating spherical pores. According to Ref. [51], quite plenty of spherical pores reside near the melting pool surface because of Marangoni convection and buoyancy forces. This kind of pores is illustrated by the blue hollow circles in Fig. 11a. When re-melting the as-solidified layer, some pores coalesce, flow towards the surface and escape. Some dissolve in the melts again as temperature increases. These pores reappear near the melting pool surface in smaller size (blue hollow circles in Fig. 11b) when temperature decreases. However, there are also some pores located at the bottom of the melting pools, indicating by orange circles. They are formed because of gas solubility reduction during rapid solidification of the solid/liquid interface at bottom. Re-melting also gives a chance for pores at bottom to float up and escape because the size of melting pools resembles that of the first routine (Fig. 11b). The pink circles in Fig. 11b represent the gas which is still entrapped in the re-melting processing. Spherical pores are also illustrated in Fig. 11c and d. The upper layer melting further reduces the spherical pores near top surface in the former layer. Therefore, when the bulk materials were re-scanned, the amount of entrapped gas goes down to a low level.

Fig. 11c illustrates the formation principles of irregular pores due to lack of fusion, marked by the red profiles. As Sample 1 suffers higher surface roughness, the powders deposited on it tend to be trapped, in particular, in between the adjacent tracks. As discussed, Ra values of the re-melting parts decrease significantly after re-scanning. Thereby, the powders deposited on the re-melting layers are more packed and uniform (see Fig. 11a and b). The melting pools of a new layer tend to submerge deeper areas of last layer, creating fewer pores lack of fusion (Fig. 11d).

4. Conclusions

Re-melting strategies with same and opposite directions to the first scanning were performed with SLM on AlSi10Mg parts. Top surface roughness decreases to almost the same level for the two scanning strategies while side surface witnessed a contradictory trend. Both directional strategies show the same trend to decrease porosity. The difference lies in the ability to release porosity at edges of the parts. Opposite direction strategy is inferior to the same direction re-melting because of the different keyhole porosity distribution at the head and wake of the melting tracks.

Acknowledgements

This research is supported by National Natural Science Foundation of China (Project No. 51371109) and National Research Foundation, Prime Minister's Office, Singapore under its Medium-Sized Centre funding scheme. Wenhui Yu appreciates the sponsorship from China Scholarship Council (Sponsorship No. 201706220205).

References

- [1] J. Li, Z. Zhao, P. Bai, H. Qu, B. Liu, L. Li, L. Wu, R. Guan, H. Liu, Z. Guo, Microstructural evolution and mechanical properties of IN718 alloy fabricated by selective laser melting following different heat treatments, *J. Alloys Compd.* 772 (2019) 861-870.
- [2] S. Fatemi, J.Z. Ashany, A.J. Aghchai, A. Abolghasemi, Experimental investigation of process parameters on layer thickness and density in direct metal laser sintering: a response surface methodology approach, *Virtual Phys. Prototyp.* 12 (2017) 133-140.
- [3] J.H. Rao, Y. Zhang, K. Zhang, A. Huang, C.H.J. Davies, X. Wu, Multiple precipitation pathways in an Al-7Si-0.6Mg alloy fabricated by selective laser melting, *Scripta Mater.* 160 (2019) 66-69.
- [4] C.Y. Yap, C.K. Chua, Z.L. Dong, Z.H. Liu, D.Q. Zhang, L.E. Loh, S.L. Sing, Review of selective laser melting: Materials and applications, *Appl. Phys. Rev.* 2 (2015) 041101.
- [5] T. Yang, T. Liu, W. Liao, E. MacDonald, H. Wei, X. Chen, L. Jiang, The influence of process parameters on vertical surface roughness of the AlSi10Mg parts fabricated by selective laser melting, *J. Mater. Process. Tech.* 266 (2019) 26-36.
- [6] D. Herzog, V. Seyda, E. Wycisk, C. Emmelmann, Additive manufacturing of metals, *Acta Mater.* 117 (2016) 371-392.
- [7] D. Carluccio, M. Bermingham, Y. Zhang, D. StJohn, K. Yang, P. Rometsch, X. Wu, M. Dargusch, Grain refinement of laser remelted Al-7Si and 6061 aluminium alloys with Tibor® and scandium additions, *J. Manuf. Process.* 35 (2018) 715-720.
- [8] J.H. Martin, B.D. Yahata, J.M. Hundley, J.A. Mayer, T.A. Schaedler, T.M. Pollock, 3D printing of high-strength aluminium alloys, *Nature* 549 (2017) 365.

- [9] L. Xi, P. Wang, K.G. Prashanth, H. Li, H.V. Prykhodko, S. Scudino, I. Kaban, Effect of TiB_2 particles on microstructure and crystallographic texture of Al-12Si fabricated by selective laser melting, *J. Alloys Compd.* 786 (2019) 551-556.
- [10] J. Haubrich, J. Gussone, P. Barriobero-Vila, P. Kürsteiner, E.A. Jägle, D. Raabe, N. Schell, G. Requena, The role of lattice defects, element partitioning and intrinsic heat effects on the microstructure in selective laser melted Ti-6Al-4V, *Acta Mater.* 167 (2019) 136-148.
- [11] D. Sun, D. Gu, K. Lin, J. Ma, W. Chen, J. Huang, X. Sun, M. Chu, Selective laser melting of titanium parts: Influence of laser process parameters on macro- and microstructures and tensile property, *Powder Technol.* 342 (2019) 371-379.
- [12] Z. Wang, Z. Xiao, Y. Tse, C. Huang, W. Zhang, Optimization of processing parameters and establishment of a relationship between microstructure and mechanical properties of SLM titanium alloy, *Opt. Laser Technol.* 112 (2019) 159-167.
- [13] S. Huang, W.Y. Yeong, Laser re-scanning strategy in selective laser melting for part quality enhancement: a review, *Proceedings of the 3rd International Conference on Progress in Additive Manufacturing (Pro-AM 2018)*, Singapore, 2018, pp. 413-419.
- [14] Q. Han, Y. Jiao, Effect of heat treatment and laser surface remelting on AlSi10Mg alloy fabricated by selective laser melting, *Int. J. Adv. Manuf. Tech.* (2019) 1-10.
- [15] X. Yang, J. Liu, X. Cui, G. Jin, Z. Liu, Y. Chen, X. Feng, Effect of remelting on microstructure and magnetic properties of Fe-Co-based alloys produced by laser additive manufacturing, *J. Phys. Chem. Solids* (2019) 210-216.

- [16] B. Liu, B.Q. Li, Z.H. Li, Selective laser remelting of an additive layer manufacturing process on AlSi10Mg, *Results Phys.* 12 (2019) 982-988.
- [17] S. Griffiths, M. Rossell, J. Croteau, N. Vo, D. Dunand, C. Leinenbach, Effect of laser rescanning on the grain microstructure of a selective laser melted Al-Mg-Zr alloy, *Mater. Charact.* 143 (2018) 34-42.
- [18] S. Zhou, Y. Xu, B. Liao, Y. Sun, X. Dai, J. Yang, Z. Li, Effect of laser remelting on microstructure and properties of WC reinforced Fe-based amorphous composite coatings by laser cladding, *Opt. Laser Technol.* 103 (2018) 8-16.
- [19] S. Campanelli, A. Angelastro, P. Posa, G. Daurelio, Fiber laser surface remelting of a nickel-based superalloy by an integrated rectangular laser spot, *Opt. Laser. Eng.* 111 (2018) 42-49.
- [20] B. He, X. Cheng, J. Li, X.-J. Tian, H.-M. Wang, Effect of laser surface remelting and low temperature aging treatments on microstructures and surface properties of Ti-55511 alloy, *Surf. Coat. Tech.* 316 (2017) 104-112.
- [21] D.P. Karmakar, M. Gopinath, A.K. Nath, Effect of tempering on laser remelted AISI H13 tool steel, *Surf. Coat. Tech.* 361 (2019) 136-149.
- [22] R. Li, Y. Jin, Z. Li, Y. Zhu, M. Wu, Effect of the remelting scanning speed on the amorphous forming ability of Ni-based alloy using laser cladding plus a laser remelting process, *Surf. Coat. Tech.* 259 (2014) 725-731.
- [23] E. Yasa, J. Deckers, J.P. Kruth, The investigation of the influence of laser re-melting on density, surface quality and microstructure of selective laser melting parts, *Rapid Prototyping J.* 17 (2011) 312-327.

- [24] E. Yasa, J.-P. Kruth, Microstructural investigation of Selective Laser Melting 316L stainless steel parts exposed to laser re-melting, *Procedia Eng.* 19 (2011) 389-395.
- [25] T. Gustmann, H. Schwab, U. Kühn, S. Pauly, Selective laser remelting of an additively manufactured Cu-Al-Ni-Mn shape-memory alloy, *Mater. Des.* 153 (2018) 129-138.
- [26] B. AlMangour, D. Grzesiak, J.M. Yang, Scanning strategies for texture and anisotropy tailoring during selective laser melting of TiC/316L stainless steel nanocomposites, *J. Alloys Compd.* 728 (2017) 424-435.
- [27] H. Ali, H. Ghadbeigi, K. Mumtaz, Effect of scanning strategies on residual stress and mechanical properties of Selective Laser Melted Ti6Al4V, *Mat. Sci. Eng. A* 712 (2018) 175-187.
- [28] K. Wei, M. Lv, X. Zeng, Z. Xiao, G. Huang, M. Liu, J. Deng, Effect of laser remelting on deposition quality, residual stress, microstructure, and mechanical property of selective laser melting processed Ti-5Al-2.5 Sn alloy, *Mater. Charact.* 150 (2019) 67-77.
- [29] C. Zhang, H. Zhu, Z. Hu, L. Zhang, X. Zeng, A comparative study on single-laser and multi-laser selective laser melting AlSi10Mg: defects, microstructure and mechanical properties, *Mat. Sci. Eng. A* 746 (2019) 416-423.
- [30] C. Weingarten, D. Buchbinder, N. Pirch, W. Meiners, K. Wissenbach, R. Poprawe, Formation and reduction of hydrogen porosity during selective laser melting of AlSi10Mg, *J. Mater. Process. Tech.* 221 (2015) 112-120.
- [31] J. Vaithilingam, R.D. Goodridge, R.J. Hague, S.D. Christie, S. Edmondson, The effect of laser remelting on the surface chemistry of Ti6Al4V components fabricated by selective laser melting, *J. Mater. Process. Tech.* 232 (2016) 1-8.

- [32] P. Krakhmalev, I. Yadroitsava, G. Fredriksson, I. Yadroitsev, In situ heat treatment in selective laser melted martensitic AISI 420 stainless steels, *Mater. Des.* 87 (2015) 380-385.
- [33] J. Zhang, B. Song, Q. Wei, D. Bourell, Y. Shi, A review of selective laser melting of aluminum alloys: Processing, microstructure, property and developing trends, *J. Mater. Sci. Technol.* 35 (2019) 270-284.
- [34] R. Li, M. Wang, T. Yuan, B. Song, C. Chen, K. Zhou, P. Cao, Selective laser melting of a novel Sc and Zr modified Al-6.2 Mg alloy: Processing, microstructure, and properties, *Powder Technol.* 319 (2017) 117-128.
- [35] M. Wang, B. Song, Q. Wei, Y. Zhang, Y. Shi, Effects of annealing on the microstructure and mechanical properties of selective laser melted AlSi7Mg alloy, *Mat. Sci. Eng. A* 739 (2019) 463-472.
- [36] E. Brandl, U. Heckenberger, V. Holzinger, D. Buchbinder, Additive manufactured AlSi10Mg samples using Selective Laser Melting (SLM): Microstructure, high cycle fatigue, and fracture behavior, *Mater. Des.* 34 (2012) 159-169.
- [37] N. Read, W. Wang, K. Essa, M.M. Attallah, Selective laser melting of AlSi10Mg alloy: Process optimisation and mechanical properties development, *Mater. Des.* 65 (2015) 417-424.
- [38] E. Louvis, P. Fox, C.J. Sutcliffe, Selective laser melting of aluminium components, *J. Mater. Process. Tech.* 211 (2011) 275-284.
- [39] W. Yu, S.L. Sing, X. Tian, C.K. Chua, Effects of re-melting strategies on densification behavior and mechanical properties of selective laser melted AlSi10Mg parts,

Proceedings of the 3rd International Conference on Progress in Additive Manufacturing (Pro-AM 2018), Singapore, 2018, pp. 476-481.

- [40] C. Qiu, H. Chen, Q. Liu, S. Yue, H. Wang, On the solidification behaviour and cracking origin of a nickel-based superalloy during selective laser melting, *Mater. Charact.* 148 (2019) 330-344.
- [41] S.L. Sing, F.E. Wiria, W.Y. Yeong, Selective laser melting of titanium alloy with 50 wt% tantalum: Effect of laser process parameters on part quality, *Int. J. Refract. Met. H.* 77 (2018) 120-127.
- [42] F. Calignano, Investigation of the accuracy and roughness in the laser powder bed fusion process, *Virtual Phys. Prototyp.* 13 (2018) 97-104.
- [43] P. Yuan, D. Gu, Molten pool behaviour and its physical mechanism during selective laser melting of TiC/AlSi10Mg nanocomposites: simulation and experiments, *J. Phys. D Appl. Phys.* 48 (2015) 035303.
- [44] K. Darvish, Z. Chen, T. Pasang, Reducing lack of fusion during selective laser melting of CoCrMo alloy: Effect of laser power on geometrical features of tracks, *Mater. Des.* 112 (2016) 357-366.
- [45] H.D. Carlton, A. Haboub, G.F. Gallegos, D.Y. Parkinson, A.A. MacDowell, Damage evolution and failure mechanisms in additively manufactured stainless steel, *Mat. Sci. Eng. A* 651 (2016) 406-414.
- [46] T. DebRoy, H.L. Wei, J.S. Zuback, T. Mukherjee, J.W. Elmer, J.O. Milewski, A.M. Beese, A. Wilson-Heid, A. De, W. Zhang, Additive manufacturing of metallic components – Process, structure and properties, *Prog. Mater. Sci.* 92 (2018) 112-224.

- [47] J. Elmer, J. Vaja, H. Carlton, R. Pong, The effect of Ar and N₂ shielding gas on laser weld porosity in steel, stainless steels, and nickel, *Weld J* 94 (2015) 313s-325s.
- [48] T. Kimura, T. Nakamoto, Microstructures and mechanical properties of A356 (AlSi7Mg0.3) aluminum alloy fabricated by selective laser melting, *Mater. Des.* 89 (2016) 1294-1301.
- [49] W.E. King, H.D. Barth, V.M. Castillo, G.F. Gallegos, J.W. Gibbs, D.E. Hahn, C. Kamath, A.M. Rubenchik, Observation of keyhole-mode laser melting in laser powder-bed fusion additive manufacturing, *J. Mater. Process. Tech.* 214 (2014) 2915-2925.
- [50] R. Xiao, X. Zhang, Problems and issues in laser beam welding of aluminum–lithium alloys, *J. Manuf. Process.* 16 (2014) 166-175.
- [51] C.L.A. Leung, S. Marussi, R.C. Atwood, M. Towrie, P.J. Withers, P.D. Lee, In situ X-ray imaging of defect and molten pool dynamics in laser additive manufacturing, *Nat. Commun.* 9 (2018) 1355.

Figure and Table Captions

Fig. 1 AlSi10Mg powders used to fabricate the SLM samples in this study.

Fig. 2 Scanning strategies of Sample 1-3.

Fig. 3 Building orientation and cutting surface of sample fabricated with SLM.

Fig. 4 Surface roughness (Ra) of top xoy and side xoz plane of Sample 1-3.

Fig. 5 Melting pool profiles for (a) Sample 1; (b) Sample 2; (c) Sample 3.

Fig. 6 Reconstructed micro-CT images (viewed from top) of (a, d) Sample 1; (b, e) Sample 2; (c, f) Sample 3. (a-c) are in perspective view, (d-f) are in parallel view.

Fig. 7 Porosity of samples within total and central areas.

Fig. 8 OM images of horizontal cross-section at edges (a) Sample 1; (b) Sample 2; (c) Sample 3.

Fig. 9 OM images of vertical (a-c) and horizontal (e-f) cross-section at central areas (a, d) Sample 1; (b, e) Sample 2; (c, f) Sample 3.

Fig. 10 Escape of keyhole porosity after re-melting at edges.

Fig. 11 Spherical and irregular porosity escape after re-melting at central areas.

Fig. S1 3D display (a-c) and microstructure (d-f) of top surfaces of (a, d) Sample 1; (b, e) Sample 2; (c, f) Sample 3. Insets on the right top of d-f are the macro profiles of top surface.

Fig. S2 The microstructure at cutting plane of (a) Sample 1; (b) Sample 2; (c) Sample 3.

Table 1 Processing parameters employed for the samples.

Table 1

Samples	Laser power (W)	Scanning speed (mm/s)	Hatch spacing (μm)	Layer thickness (μm)	Scanning strategy	Re-melting direction
Sample 1						N.A.
Sample 2	350	1150	170	50	Bi-directional	Same direction
Sample 3						Opposite direction

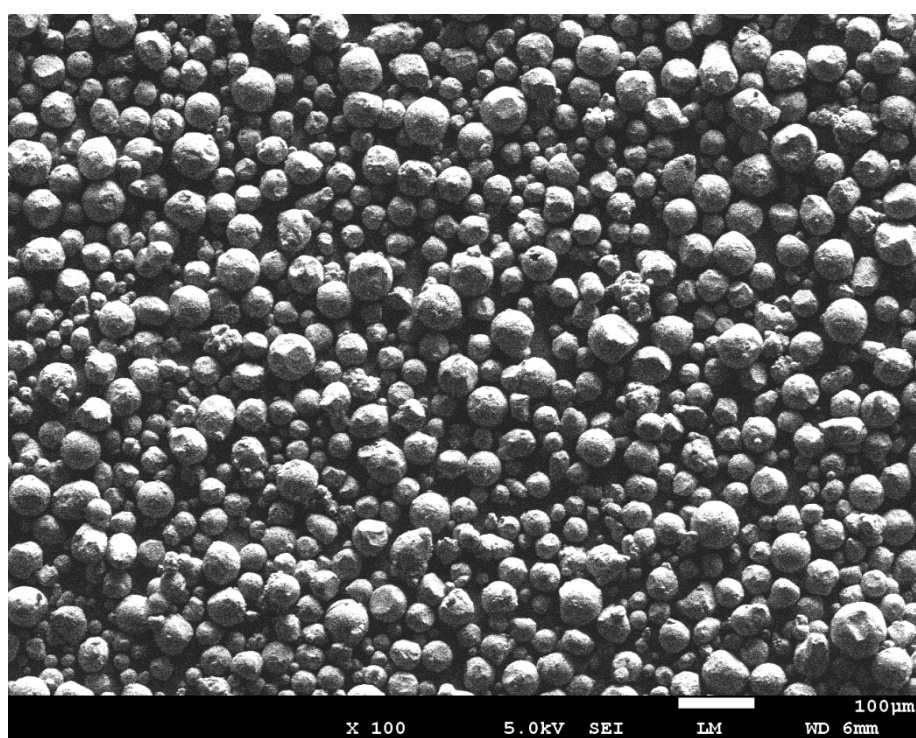


Fig. 1

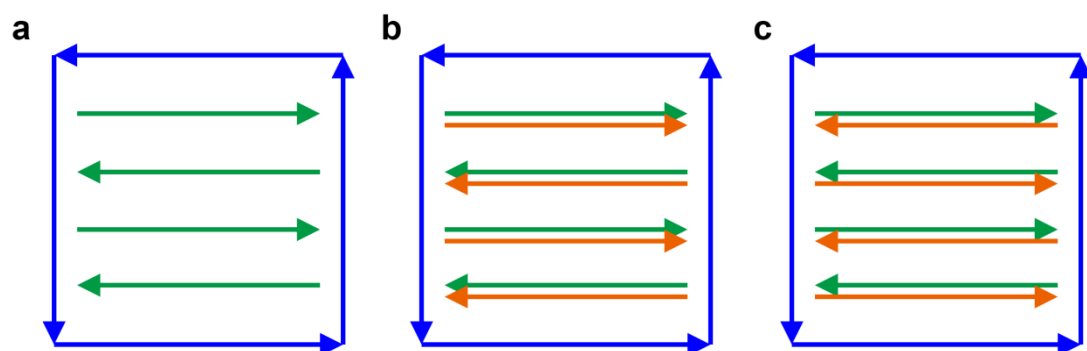


Fig. 2

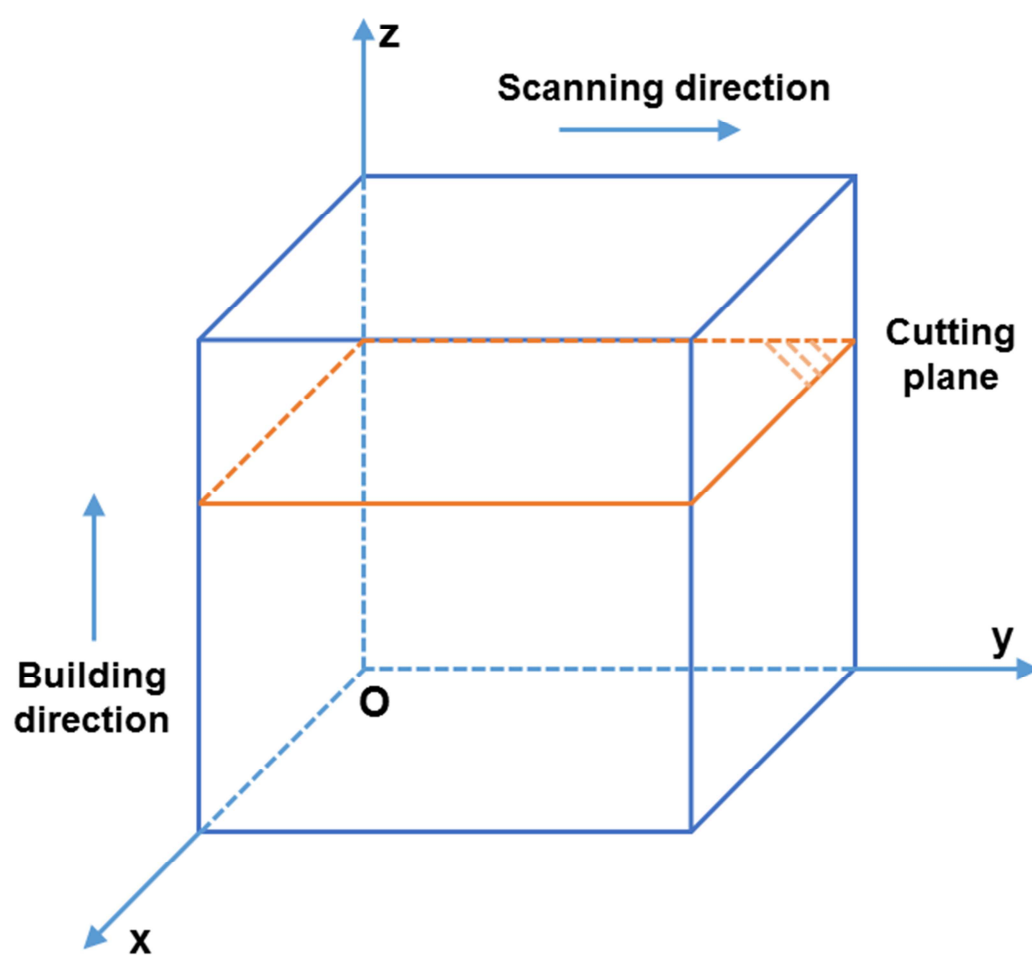


Fig. 3

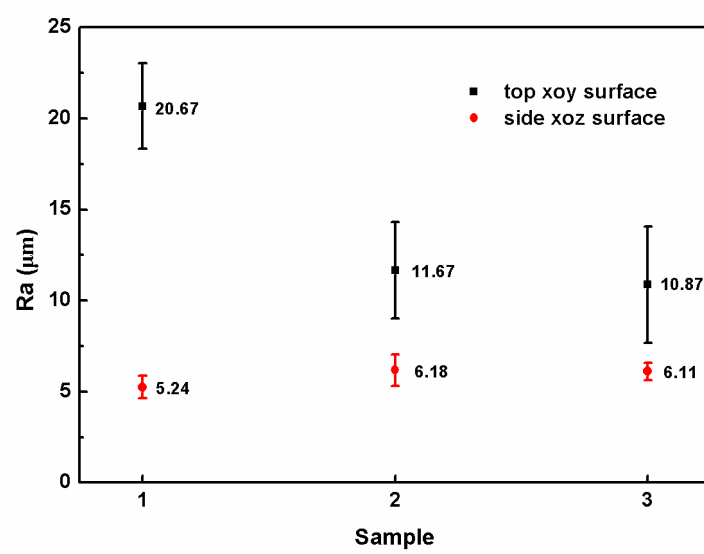
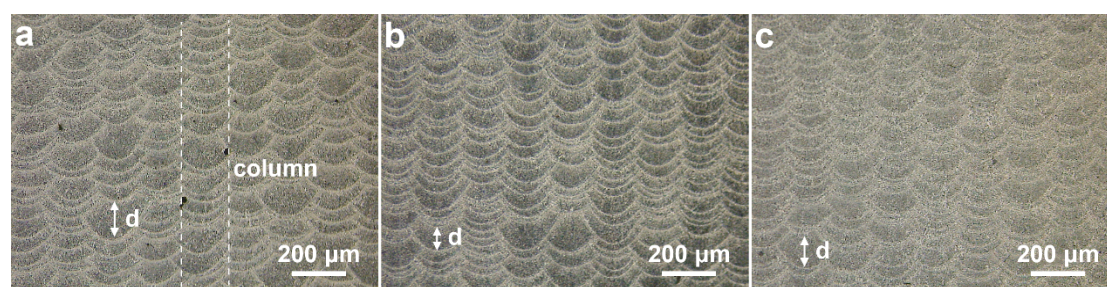
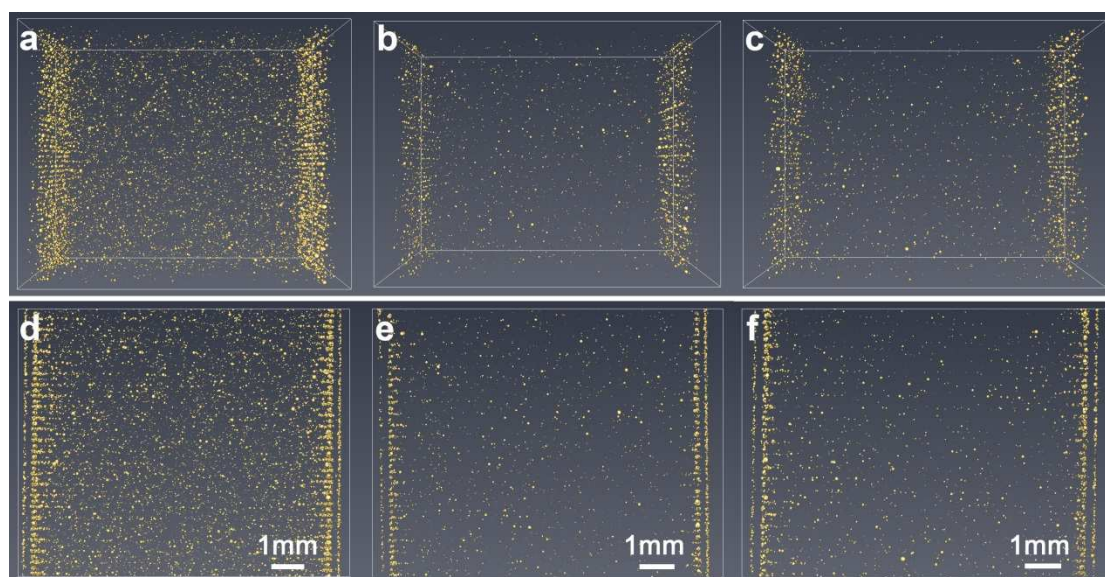


Fig. 4

**Fig. 5**

**Fig. 6**

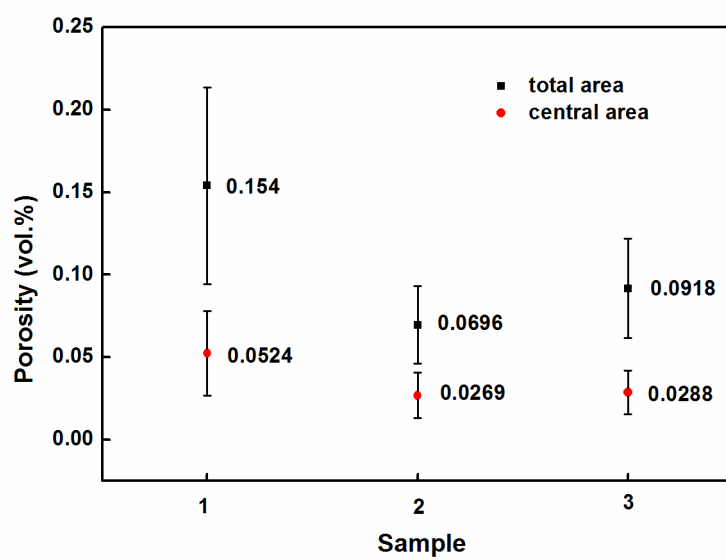


Fig. 7

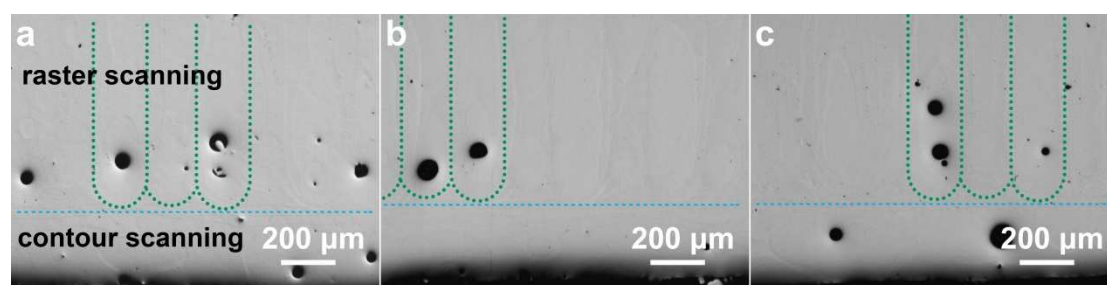
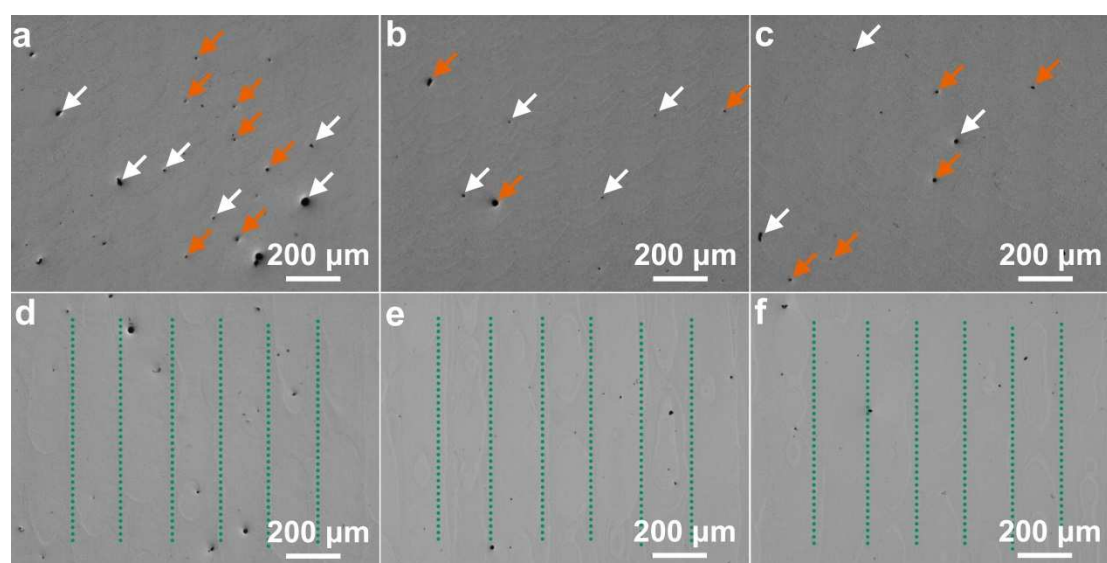


Fig. 8

**Fig. 9**

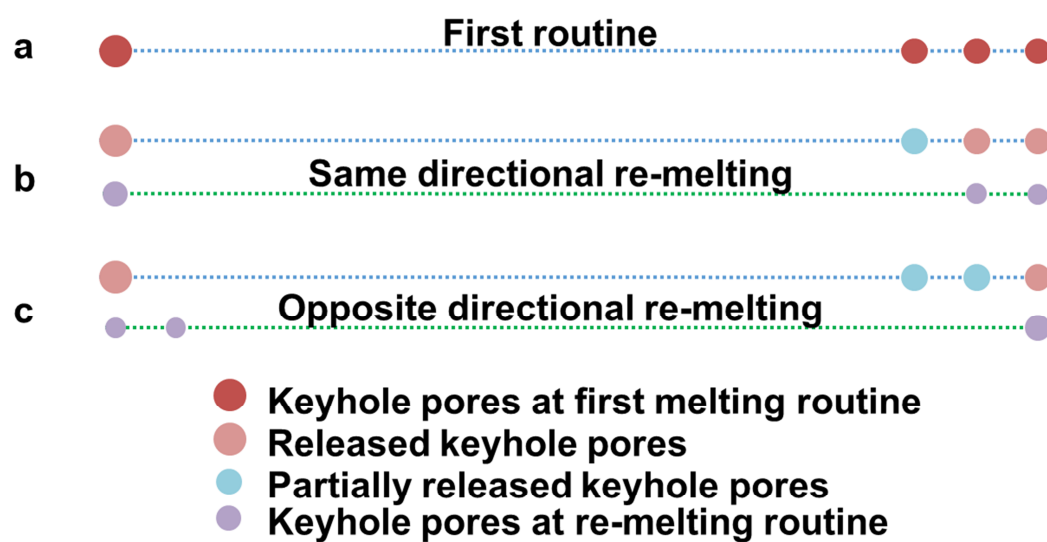


Fig. 10

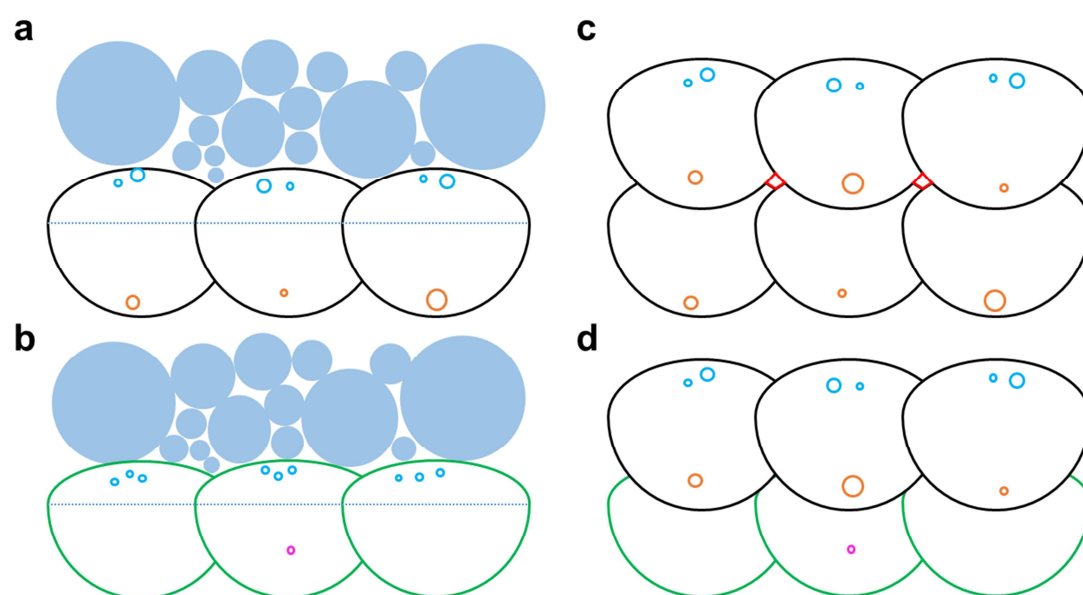


Fig. 11

1. Surface roughness decreases on top surface but increases on side surface after re-melting.
2. Same directional re-melting releases more keyhole pores at edges.
3. Pores release efficiency is the same for same and opposite re-melting directions.